

# Constraining FRB Microstructure with Polarised Shot Noise

J. C. F. Balzan,<sup>1</sup> A. Bera,<sup>2,1</sup> C. W. James,<sup>1</sup> and B. W. Meyers<sup>3,1</sup>

<sup>1</sup>International Centre for Radio Astronomy Research (ICRAR), Curtin University, Bentley, WA 6012, Australia

<sup>2</sup>ASTRON, Netherlands Institute for Radio Astronomy, Postbus 2, 7990 AA Dwingeloo, Netherlands

<sup>3</sup>Australian SKA Regional Centre (AusSRC), Curtin University, Kent Street, Bentley, WA 6102, Australia

**Author for correspondence:** J. C. F. Balzan, Email: joel.balzan@icrar.org.

(Received dd Mmm YYYY; revised dd Mmm YYYY; accepted dd Mmm YYYY; first published online 22 September 202X)

## Abstract

We present FIRES, a polarised shot-noise framework that models fast radio burst (FRB) dynamic spectra as the incoherent superposition of Gaussian microshots. Applied to the CRAFT bursts FRB 20191001A and FRB 20240318A, FIRES reproduces key spectro-polarimetric behaviours: scattering suppresses position-angle (PA) variability on the trailing edge, while the leading edge preferentially retains intrinsic structure when sufficient signal-to-noise is present. We quantify this behaviour using the PA variance ratio  $\mathcal{R}_\psi$  and explore the joint plane of measured linear polarisation fraction  $\Pi_L$  versus PA variance to constrain the allowed parameter space of microshot number  $N$ , intrinsic PA dispersion  $\sigma_\psi$ , and intrinsic linear fraction  $\Pi_{L,0}$  at fixed signal-to-noise. For FRB 20191001A, the data are consistent with an extended region spanning  $\sigma_\psi \sim 10^\circ\text{--}30^\circ$  and  $N \sim 5\text{--}1000$ , reflecting degeneracies between intrinsic PA structure, microshot superposition, scattering, finite sampling, and noise. FRB 20240318A occupies a more restricted region, favouring fewer microshots ( $N \lesssim 20$ ) and larger intrinsic PA dispersion ( $\sigma_\psi \sim 15\text{--}23^\circ$ ), depending on  $\Pi_{L,0}$ , consistent with its observed PA variability. By combining an emission-mechanism-independent framework with minimal assumptions and observational constraints, FIRES provides direct, quantitative constraints on the space of viable FRB microphysical models and demonstrates that microshot superposition offers a natural explanation for the diverse polarimetric behaviours observed in FRBs.

**Keywords:** XXXXXXXXXXXXXXXX

## 1. INTRODUCTION

Fast Radio Bursts (FRBs) are transient radio signals characterised by their short duration and high brightness temperatures (Lorimer et al., 2007). The FRB population is diverse, exhibiting various properties such as apparent “one-off” events or strong repeaters (see Petroff et al., 2019, 2022, for recent reviews), highly variable polarisation angles (PAs), linear and circular polarisation fractions, rotation measures (RMs), as well as complex temporal and spectral profiles with multiple peaks and varying widths (e.g., Sherman et al., 2024; Sand et al., 2025; Scott et al., 2025). The study of these structures is essential for deciphering FRB generation mechanisms and the media through which they propagate.

FRBs show diverse PA behaviour. Only one FRB is well fit by a rotating vector model (McKinven et al., 2025), a characteristic of a rotating neutron star, with circumstantial evidence for two more (Bera et al., 2024). Others show a variety of PA swings (Luo et al., 2020), or macroscopically flat PA profiles (e.g., Pandhi et al., 2024). The Canadian Hydrogen Mapping Experiment (CHIME) and the Deep Synoptic Array 110 (DSA-110) previously categorised FRBs by their spectro-temporal morphology (Pleunis et al., 2021; Sand et al., 2025), macroscopic PA features (Pandhi et al., 2024) and their polarisation fractions (Sherman et al., 2024). These are highly dependent on S/N, time resolution, and propagation effects and leads to arbitrary classifications as suggested by Scott et al. (2025). Studying macroscopic PA features may be beneficial in identifying rotational signatures or probing large-scale, spa-

tially averaged magnetic field structures, and can inform us of potential progenitors; however, they provide limited insight of the smaller-scale processes that likely drive FRB emission.

Scott et al. (2025) present high-time-resolution (HTR) polarisation properties of 35 FRBs from the Commensal Real-time ASKAP Fast Transients (CRAFT) Survey. They move away from previous classifications, showing that all FRBs likely have multiple components and have intrinsically variable PAs. However, measuring these temporal structures can be influenced by several factors, including the intrinsic properties of the source and its environment, and particularly scattering along the line of sight. When sampled with HTR, FRBs with little-to-no scattering and high signal-to-noise (S/N) can exhibit complex, narrow intrinsic widths (nanoseconds–microseconds; Nimmo et al., 2022) and highly variable PAs within the burst envelope (e.g., Gupta et al., 2022; Snelders et al., 2023; Scott et al., 2025). Observations of these structures can place stringent constraints on the size of the emitting region and emission mechanisms of FRBs, as well as the various propagation media (e.g. Beniamini & Kumar, 2020).

The idea of radio pulses being comprised of multiple smaller “shots” was first suggested by Rickett (1975) in the amplitude-modulated noise model for pulsars. This idea was extended by Cordes (1976) who implemented polarisation variations to explain short-time scale polarisation structures. Many further developments have since been made to the model to account for stochastic processes (e.g., Melrose & Macquart, 1998; McKinnon, 2006; Olsowski et al., 2011). The most famous applica-

tion of the shot-models is to the Crab pulsar, which displays nanosecond duration shots (nanoshots) with PA microstructure (Hankins & Eilek, 2007; Hankins *et al.*, 2016). Nimmo *et al.* (2022) and Scott *et al.* (2025) similarly note that their FRB samples have structures resembling Crab nanoshots.

Of the Crab pulsar's many components, single pulses in the main pulse and interpulse exhibit similar polarimetric nanosstructure to FRBs. They often appear completely unpolarised at time resolutions of the the order of 10's of  $\mu\text{s}$ – $\text{ms}$ , but, at nanosecond time resolution minimal scattering, they appear to be resolved to 100% polarised nanoshots with random PAs (Hankins *et al.*, 2015, 2016). Hankins *et al.* (2016) show that unresolved microbursts generally have highly disordered PA profiles, consistent with shots having random PAs. Occasionally their PAs show ordered swings (see their Figure 4) which may trace underlying plasma or magnetic field structures from the emission environment. They also show that microbursts are in fact unresolved collections of narrow-band nanoshots, with some demonstrating substructures of timescales less than 4 ns (see their Figure 8). This behaviour is consistent with expectations from the PSN model. Giant pulses (GPs) are a subclass of single pulses with luminosities several orders of magnitude greater than the average pulses, a distinct energy distribution (power law), and a narrow emission phase window (compared to the average pulse profile). In terms of duration and energetics, Crab GPs and their underlying nanoshot mechanism are the most analogous phenomena to FRBs (e.g., Nimmo *et al.*, 2022). These Crab phenomena each show intense PA variability on nanosecond to microsecond timescales (e.g., Jessner *et al.*, 2010; Hankins *et al.*, 2016) and a variety of spectro-temporal morphologies, on durations similar to FRBs observed at very-high time resolution.

A natural question is whether depolarisation in FRBs may arise from the superposition of many microshots, analogous to the behaviour of Crab microbursts. Other contributors include depolarisation from scattering, Faraday rotation through turbulent media, or the intrinsic emission mechanism itself. Disentangling these possibilities requires controlled forward modelling of FRB microstructure and polarisation at high time resolution. However, the current sample of high-S/N, low-scatter FRBs with nanosecond–microsecond resolution remains limited, motivating the need for realistic simulations.

Several existing packages offer pulsar-signal simulation capabilities (e.g., Hotan *et al.*, 2004; Hazboun *et al.*, 2021), but these are generally unsuited to FRBs because they model emission profiles with simple Gaussian components and lack polarisation-analysis tools. In this paper, we introduce the Fast, Intense Radio Emission Simulator (FIRES),<sup>a</sup> a Python package for simulating and analysing FRB dynamic spectra as ensembles of microshots with intrinsically varied properties. We demonstrate how FIRES can reproduce key observed FRB properties — including PA variance, depolarisation behaviour, and linear polarisation fraction — and show how microshot superposition can naturally generate the diversity of polarimetric structures seen in FRBs.

<sup>a</sup><https://github.com/JoeBalzan/FIRES>

## 2. MODELLING DYNAMIC SPECTRA

Following the idea that all FRBs intrinsically have multiple components (Scott *et al.*, 2025), we model the dynamic spectra of FRBs as a superposition of Gaussian microshots (polarised shot noise; Cordes, 1976) using FIRES. Each microshot is defined by its amplitude, time of arrival (TOA), width, PA, and polarisation fractions, with the latter specifying that each microshot is partially elliptically polarised. For our initial model, we assume that each microshot has a Gaussian intensity profile with a constant peak and that their TOAs are distributed normally, and we ignore frequency dependence in intrinsic power. Each microshot has its full-width half-maximum (FWHM) sampled from a uniform distribution, its PA sampled from a normal distribution, and all other parameters are fixed. The microshots are then scattered by convolution with a thin-screen scattering response, diffractive interstellar scintillation (DISS) is applied as a multiplicative gain field, and noise is added to create realistic FRB dynamic spectra. FIRES can apply Faraday rotation and PA trends, however, we do not use them here. The list of parameters used in the model are presented in Table 1.

The Stokes I dynamic spectrum, comprised of  $N$  microshots in time  $t$  (ms) and frequency  $\nu$  (MHz), is

$$D_I[t, \nu] = \left[ \sum_{i=1}^N A_i \exp\left(-\frac{(t - t_i)^2}{2\sigma_{w,i}^2}\right) \right] * h_\nu(t),$$

$$\sigma_{w,i} = \frac{w_i}{2\sqrt{2\log 2}},$$

where  $*$  denotes convolution in time with the frequency-dependent, thin-screen scattering response  $h_\nu(t)$ . Each microshot has a peak amplitude  $A_i$  (arb.) and a Gaussian FWHM  $w_i = f_i W_0$ , where  $W_0$  (ms) is the envelope FWHM and the dimensionless width fraction  $f_i$  is drawn from

$$f_i \sim \mathcal{U}(f_{\min}, f_{\max}), \quad (1)$$

with  $f_{\min}$  and  $f_{\max}$  the minimum and maximum fractional widths, respectively.  $t_i$  is the arrival time of the  $i$ -th microshot, which is distributed as  $t_i \sim \mathcal{N}(t_0, \sigma_t)$ , where  $t_0$  is the arrival time of the envelope, and

$$\sigma_t = \frac{W_0}{2\sqrt{2\log 2}}. \quad (2)$$

With per-microshot polarisation angles  $\psi_i \sim \mathcal{N}(\psi_0, \sigma_\psi)$  and fixed intrinsic fractional linear and circular polarisations  $\Pi_{L,0}$  and  $\Pi_{V,0}$ , we write

$$D_Q[t, \nu] = D_I[t, \nu] \cdot \Pi_{L,0} \cdot \cos(2\psi_i),$$

$$D_U[t, \nu] = D_I[t, \nu] \cdot \Pi_{L,0} \cdot \sin(2\psi_i),$$

$$D_V[t, \nu] = D_I[t, \nu] \cdot \Pi_{V,0}.$$

### 2.1 Thin-Screen Scattering

We apply scattering via a discrete, causal impulse response per frequency channel. The continuous thin-screen scattering

**Table 1.** Model parameters used in FIRES.

Parameter	Description	FRB 20191001A	FRB 20240318A
$N$	Number of microshots	100	100
$A$ (arb.)	Peak amplitude of microshots	0.20	0.19
$t_i$ (ms)	TOA of $i$ th microshot, $t_i \sim \mathcal{N}(t_0, \sigma_t)$	$\mathcal{N}(t_0, \sigma_t)$	$\mathcal{N}(t_0, \sigma_t)$
$w_i$ (ms)	Microshot FWHM, sampled via Eq. (1)	sampled	sampled
$\sigma_{w,i}$ (ms)	Gaussian width, $\sigma_{w,i} = w_i / (2\sqrt{2\ln 2})$	derived per $w_i$	derived per $w_i$
$W_0$ (ms)	Envelope FWHM	0.50	0.06
$\sigma_t$ (ms)	Envelope width, $\sigma_t = W_0 / (2\sqrt{2\ln 2})$	0.212	0.0255
$w_{\min}$ (% of $W_0$ )	Min. microshot width fraction	5	20
$w_{\max}$ (% of $W_0$ )	Max. microshot width fraction	5	20
$t_0$ (ms)	Envelope reference TOA	fixed	fixed
$\Psi_0$ (deg)	Mean intrinsic PA	20	0
$\sigma_{\Psi}$ (deg)	PA scatter	30	10
$\Pi_{L,0}$	Intrinsic frac. linear pol.	0.95	0.83
$\Pi_{V,0}$	Intrinsic frac. circular pol.	-0.05	-0.17
$\nu_{\tau}$ (MHz)	Reference freq. for scattering & scintillation	1000	1000
$\tau_0$ (ms)	Scattering timescale at $\nu_{\tau}$	$1.78^a \pm 0.04$	$0.128^a \pm 0.005$
$\alpha$	Scattering index	$-4.85^a \pm 0.3$	$-3.22^a \pm 0.005$
$\nu_s$ (MHz)	Scintillation decorrelation bandwidth	1.5	$4^a \pm 0.2$
$t_s$ (s)	Scintillation timescale	300	300
$N_{\text{im}}$	Number of images in scattering disk	5000	5000
$\Theta_{\text{lim}}$ (dimensionless) <sup>b</sup>	Angular limit of scattering disk	3	3
SEFD (arb.)	System equivalent flux density	1.2	1.4
$\delta\nu$ (MHz)	Channel bandwidth	1	1
$\delta t$ (ms)	Time resolution	0.023	0.003

<sup>a</sup> Data from Scott et al. (2025).

<sup>b</sup> Defined in units of the characteristic scattering angle (see Section 2.2).

response is

$$h_{\nu}(t) = \frac{1}{\tau_{\nu}} e^{-t/\tau_{\nu}} H(t),$$

with Heaviside step  $H(t)$  and timescale  $\tau_{\nu}$ . Let  $\delta t$  be the time resolution and let

$$n \equiv \left\lceil 5 \frac{\tau_{\nu}}{\delta t} \right\rceil + 1$$

be the number of kernel samples. Then the implemented kernel is the truncated, sum-normalised exponential

$$\begin{aligned} \text{IRF}_{\nu}[k] &= \frac{e^{-k\delta t/\tau_{\nu}}}{\sum_{k=0}^{n-1} e^{-k\delta t/\tau_{\nu}}} \\ &= \frac{(1 - e^{-\delta t/\tau_{\nu}}) e^{-k\delta t/\tau_{\nu}}}{1 - e^{-n\delta t/\tau_{\nu}}}, \quad k = 0, \dots, n-1, \end{aligned}$$

so that  $\sum_{k=0}^{n-1} \text{IRF}_{\nu}[k] = 1$  (preserving flux), where  $k$  indexes the  $k$ -th discrete time sample. We zero-pad each time series on the right by  $(n-1)$  samples, perform a linear (FFT) convolution, and truncate to the original timespan; any power beyond the simulated window is discarded.

The frequency-scaled scattering timescale is

$$\tau_{\nu} = \tau_0 \left( \frac{\nu}{\nu_{\tau}} \right)^{\alpha}, \quad (3)$$

with reference  $\nu_{\tau} = 1$  GHz, frequency dependence  $\alpha$ , and  $\tau_0$  the timescale at the reference frequency in milliseconds.

## 2.2 Scintillation

We include DISS as a multiplicative gain field  $G(t, \nu)$  applied to all Stokes vectors. We generate a complex electric field  $E(t, \nu)$  using `ScintillationMaker`<sup>b</sup> with four control parameters: the decorrelation bandwidth  $\nu_s$ , characteristic timescale  $t_s$ , number of images drawn from the scattering disk  $N_{\text{im}}$ , and the (dimensionless) angular extent of the scattering disk  $\Theta_{\text{lim}}$ , defined in units of the characteristic scattering angle (so that  $\Theta_{\text{lim}} = 3$  corresponds to sampling the disk out to  $\sim 3\sigma$ ). In our simulations we set  $t_s = 300$  s,  $N_{\text{im}} = 5000$ , and  $\Theta_{\text{lim}} = 3.0$  to adequately sample the scattering disk and produce a realistic scintillation pattern while keeping computations manageable.  $\nu_s$  is taken from Scott et al. (2025) when available, otherwise it is chosen by eye to best mimic a real FRB. The observed intensity gain is

$$G(t, \nu) \equiv \frac{|E(t, \nu)|^2}{\langle |E(t, \nu)|^2 \rangle_{t, \nu}},$$

<sup>b</sup><https://github.com/SprengerT/ScintillationMaker/tree/main>

so that  $\langle G \rangle = 1$  over the simulated  $(t, \nu)$  grid (preserving mean flux). The scintillated Stokes parameters are then

$$D_X^{(\text{DISS})}(t, \nu) = G(t, \nu) D_X(t, \nu), \quad X \in \{I, Q, U, V\}.$$

### 2.3 Noise

To mimic telescope noise, we add Gaussian noise to the dynamic spectra with

$$\varepsilon_X(t, \nu) \sim \mathcal{N}(0, \sigma),$$

where  $\sigma$  is the noise level calculated from the radiometer equation,

$$\sigma_X = \frac{\text{SEFD}}{\sqrt{n_{\text{pol}} \delta \nu \delta t}}. \quad (4)$$

SEFD is the system equivalent flux density in arb. units,  $n_{\text{pol}} = 2$  is the number of polarisations “recorded,”  $\delta \nu$  is the frequency resolution in Hz, and  $\delta t$  is the time resolution in seconds. The observed Stokes are

$$D_X \leftarrow D_X^{(\text{DISS})} + \varepsilon_X, \quad X \in \{I, Q, U, V\}.$$

### 2.4 Polarisation Angles

We calculate the final PAs and their errors as performed by Day et al. (2020) and similarly de-bias the linear polarisation following (the typographically corrected) Equation 11 in (Everett & Weisberg, 2001),

$$L_{\text{de-bias}} = \begin{cases} \sigma_L \sqrt{\frac{L_{\text{meas}}}{\sigma_L}^2 - 1}, & \frac{L_{\text{meas}}}{\sigma_L} \geq 1.57 \\ 0, & \text{otherwise,} \end{cases}$$

except using  $\sigma_L$  instead of  $\sigma_I$  to accommodate cases where  $\sigma_I \neq \sigma_Q \neq \sigma_U$ . Further, we discard  $\psi$  where  $L_{\text{de-bias}} < 2\sigma_L$ , along with those outside the on-pulse region, the minimum boxcar width that contains 95% of the flux in the pulse profile. If PA values are in a sequence of length  $< 5$ , then we also discard them.

## 3. REPRODUCING REAL FRB STRUCTURES

Figure 1 shows the dynamic spectra of three stages of a FIRES simulation. Starting with a noiseless, unscattered FRB comprised of  $N = 100$  microshots with a uniform distribution of widths ranging from 25–100  $\mu\text{s}$  (see Equation (1)); the FWHM of the full envelope is 0.5 ms. Then we add scattering,  $\tau_{1\text{ GHz}} = 1.78$  ms and scintillation decorrelation bandwidth  $\nu_s = 1.5$  MHz with characteristic timescale  $t_s = 300$  s, and draw the phase screen with  $N_{\text{im}} = 5000$  images and truncation parameter  $\theta_{\text{lim}} = 3.0$ . Then we add noise (SEFD = 1.2 Jy, see Equation (4); on-pulse S/N = 213), and finally compare to real CRAFT FRB 20191001A data reproduced from Scott et al. (2025) with ILEX<sup>c</sup> (on-pulse S/N = 194, corrected for RM = 53.47 rad m<sup>-2</sup>). The simulated dynamic spectra are generated over a frequency range 751.5–900.5 MHz with 1 MHz

resolution, and a time resolution of 0.023 ms chosen such that (the real) FRB 20191001A has a peak S/N  $\sim 20$ . The frequency dependence for scattering is  $\alpha = -4.85$ . Post-processing measurements of the on-pulse polarisation fractions show  $\Pi_L = 0.55$  and  $\Pi_V = -0.05$ . We assume that, intrinsically, each microshot is close to 100% polarised, and so we set  $\Pi_{L,0} = 0.95$  and  $\Pi_{V,0} = -0.05$  (similar to crab nanoshots, Hankins et al., 2016). Their PAs are drawn from  $\mathcal{N}(20.0 \text{ deg}, 30.0 \text{ deg})$ .  $\tau_{1\text{ GHz}}$  and  $\alpha$  are taken from Table 2 of Scott et al. (2025), while the rest of the parameters are estimates made by-eye to mimic the properties of FRB 20191001A. Clearly, FIRES produces a visually similar result to a real FRB. The full list of model parameters are presented in Table 1.

### 3.1 Polarisation Angle Variance

FRBs show variable PA properties (e.g., Luo et al., 2020; Mckinven et al., 2025), and when probed at high time resolutions, reveal systematic fluctuations (Nimmo et al., 2021; Hewitt et al., 2023; Scott et al., 2025). It has been suggested that the strength and duration of these PA microstructures may correspond to the magnetic field conditions in the emission environment (e.g., Scott et al., 2025), and so, disentangling intrinsic and extrinsic PA fluctuations is crucial for constraining emission models. Propagation effects such as scattering introduce frequency- and time-dependent effects that obfuscate intrinsic FRB structures, and so, determining under what conditions and which portions of the FRB dynamic spectra still contain original properties is also important.

Figure 1 shows that the PA of the simulated bursts is not constant, but varies with time, scattering timescale, and noise. We define two regions in the on-pulse phase (light-blue-shaded region); the leading region is from the onset of the on-pulse to and including the peak of the burst, and the trailing region is from the peak to the end of the on-pulse. As expected, scattering flattens the PA throughout the trailing region of the burst, reducing intrinsic variability (Li & Han, 2003), while the leading region comparatively remains largely unchanged. The introduction of noise dominates the macrostructure, introducing higher PA variance in the trailing edge.

To quantify the effects of scattering on PA in different burst regions, we introduce the metric,

$$\mathcal{R}_\psi = \frac{\mathbb{V}(\psi)}{\mathbb{V}(\psi_i)}, \quad (5)$$

where  $\mathbb{V}(\psi)$  is the PA variance across the on-pulse phase and  $\mathbb{V}(\psi_i)$  is the PA variance across the individual microshots that form the FRB. This parameter quantifies how much of the intrinsic microshot PA variance remains after taking their superposition. We can approximate the expected (noiseless) PA variance in deg.<sup>2</sup> with,

$$\mathbb{V}_{\text{exp}}(\psi) = \frac{\sigma_\psi^2}{N} \left( \frac{W_{\text{tot}}}{w_{\text{tot}}} - 1 \right) \left( \frac{180}{\pi} \right)^2 \quad (6)$$

where  $W_{\text{tot}}$  and  $w_{\text{tot}}$  are the envelope and microshot FWHMs after scattering. We derive this expression in Appendix 1. This

<sup>c</sup><https://github.com/tdial2000/ILEX/tree/main>

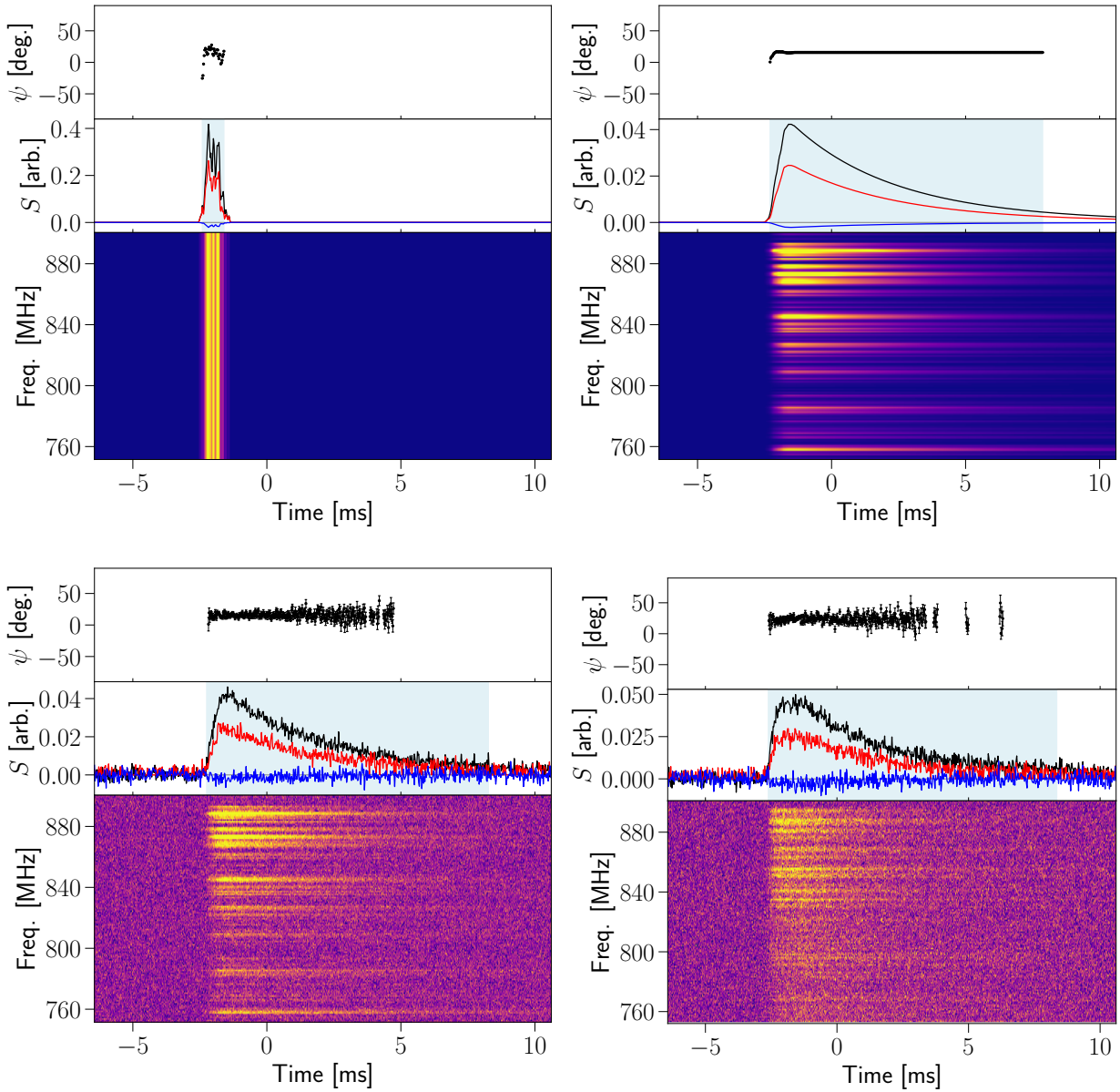


**Figure 1.** A FIRES recreation of FRB 20191001A. (a): a noiseless, unscattered FRB comprised of 100 microshots. The bottom panel is the time-frequency dynamic spectrum, the middle panel is the frequency-summed pulse profile (black = total intensity, red = linear polarisation, blue = circular polarisation), and the top panel is the polarisation angle profile. (b): scattering timescale  $\tau_{1\text{ GHz}} = 1.78$  ms and scintillation added to the top left plot (on-pulse S/N= 196). (c): noise added to the top right plot. (d): real FRB 20191001A data reproduced from Scott et al. (2025) (on-pulse S/N= 194, RM corrected from RM=53.47 rad m $^{-2}$ ). The full list of parameters used are presented in Table 1 and are described in Section 2. The top panels show the polarisation angle, the centre panels show the pulse profile, and the bottom panels show the dynamic spectra. The blue shaded regions in the centre panels is the minimum boxcar width that contains 95% of the total flux in the pulse profile.

approximation is only accurate for cases with high S/N and low  $\sigma_\psi$ . Substituting this into Equation (5), we can find the expected value of  $\mathcal{R}_\psi$ .

In Figure 2 we show how  $\mathcal{R}_\psi$  modulates as a function of the input scattering timescale,  $\tau_0$ , weighted by the input FWHM of the envelope,  $W_0$ , for different frequency bands and phase regions of a high S/N case of the simulated FRB shown in Figure 1c.  $\mathcal{R}_\psi$  exhibits three regimes. In the negligible-scattering regime,  $\mathcal{R}_\psi$  remains constant with  $\tau_0$ , since the scattering timescale is small compared to the intrinsic PA vari-

ation timescales (i.e., the width of each microshot). As  $\tau_0$  increases,  $\mathcal{R}_\psi$  then decreases, as scattering blends random microshots together, reducing the variance. At very large  $\tau_0$ , noise begins to dominate and variance increases. As expected,  $\mathcal{R}_\psi$  in the lower frequency band is initially lower due to the frequency dependence of scattering, but becomes higher at large  $\tau_0$  once the PA is flattened by scattering and noise dominates. The trailing region follows the same trend but is more strongly affected by scattering, leading to a more rapid decline in  $\mathcal{R}_\psi$ . Similarly, the highest-quarter and full-band with total-

phase, also decrease as they become scatter dominated, but transition to the noise-dominated regime at larger  $\tau_0$  owing to their higher S/N.

By contrast, the leading edge consistently retains a larger fraction of the intrinsic PA variance at increasing scattering timescales. In high S/N cases, this makes the leading edge the most robust phase region for preserving information about the intrinsic PA structure, and therefore the most informative probe of the initial emission and generation conditions.

The black dotted line shows the expected value of  $\mathcal{R}_\psi$  (Equation (6)) in the noiseless regime and is in general agreement with all regions in the low-scattering, high-S/N limit.

### 3.2 Linear Polarisation Fraction

FRBs generally exhibit high linear polarisation fractions (Sherman *et al.*, 2024; Pandhi *et al.*, 2024; Scott *et al.*, 2025), and so it has been thought that all FRBs are intrinsically 100% linearly polarised, with any depolarisation or polarisation conversion occurring due to rotation measure (RM) scattering (Feng *et al.*, 2022; Uttarkar *et al.*, 2025). However, Sand *et al.* (2025) and Scott *et al.* (2025) show no correlation between scattering and polarisation fraction. Further, Scott *et al.* (2025) rule out depolarisation due to unresolved, random PA structures as there is no correlation between decreases in linear polarisation fraction and PA fluctuations. Sherman *et al.* (2024) also suggest that this case may be less significant than propagation effects.

Figure 1 clearly shows evidence of depolarisation due to the superposition of random PAs. The intrinsic microshot polarisation fractions are  $\Pi_{L,0} = 0.95$  and  $\Pi_{V,0} = -0.05$ ; however, when superimposing  $N = 100$  microshots with PAs sampled from a normal distribution with a standard deviation of  $\sigma_\psi = 30^\circ$ , then  $\Pi_L \ll 0.95$ .

We illustrate this for the leading edge (see Section 3.1) of FRB 20191001A in Figures 3a,b where we sweep  $\sigma_\psi = 0\text{--}45^\circ$  for different values of  $N$ . Starting with  $N = 5$  in Figure 3a, the left-most point corresponds to  $\sigma_\psi = 0^\circ$ , and the right-most point corresponds to  $\sigma_\psi = 45^\circ$ . At  $\sigma_\psi = 0^\circ$  the intrinsic PA profile is completely flat, no depolarisation due to microshot superposition occurs and so  $\Pi_L = \Pi_{L,0} = 0.95$ . Here the only contribution to  $\mathbb{V}(\psi)$  is from noise, as described by Equation (4) which determines the minimum  $\mathbb{V}(\psi)$  for all values of  $N$  at  $\sigma_\psi = 0^\circ$ . As we increase  $\sigma_\psi$ ,  $\mathbb{V}(\psi)$  increases and microshots with different PAs start overlapping, causing a reduction in  $\Pi_L$ . As we move to larger values of  $N$ , we increase the effective shot-rate ( $N_{\text{eff}}$  shots  $s^{-1}$ ; see Section Appendix 1) since the envelope width,  $W_0$ , remains constant. So, as  $N$  increases, microshots overlap more often and stronger depolarisation occurs for a given  $\sigma_\psi > 0$ . This also means that, since more averaging of PAs occurs,  $\mathbb{V}(\psi)$  decreases for a given  $\sigma_\psi > 0$ . If we decrease  $\Pi_{L,0}$ , we decrease our signal in  $L$  and noise becomes more significant. So a decrease in  $\Pi_{L,0}$  also corresponds to an increase in  $\mathbb{V}(\psi)$  which we see when comparing to Figure 3b where we have reduced  $\Pi_{L,0}$  to 0.6. We now see how we might reproduce intrinsic parameters of FRB 20191001A with this model.

We show the same analysis for FRB 20240318A in Fig-

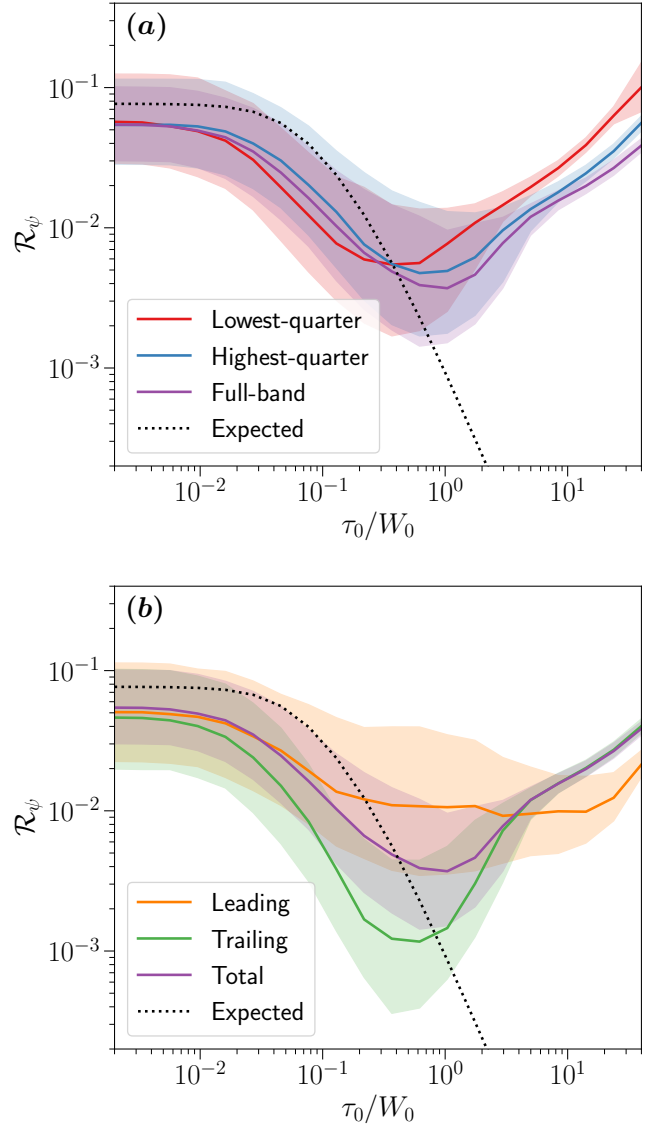


**Figure 2.**  $\mathcal{R}_\psi$  (see Equation (5)) versus  $\tau_0$  weighted by initial Gaussian envelope width,  $W_0$ , for a high S/N case of the mock FRB 20191001A (Figure 1c). The solid lines are the median value of 500 random FRB realisations at each scattering timescale, and the shaded regions represent the 16th and 84th percentiles of the realisations. The black-dotted line is the (noiseless) expected value from Equation (6). (a): frequency band comparison; The red line is the contribution from the lowest quarter of the band, the blue line is the contribution from the highest quarter of the band, and the purple line is the contribution from the full band. (b): phase comparison; The orange line is the contribution from the first half of the burst, the green line is the contribution from the second half of the burst, and the purple line is the contribution from the entire burst. At  $\tau_0/W_0 = 0, 20$ ,  $S/N = 3188, 241$ , respectively.

ures 3c,d and 4 using the parameters listed in Table 1. Post-processing measurements of the on-pulse polarisation fractions in 4b show  $\Pi_L = 0.78$  and  $\Pi_V = -0.17$ .

## 4. DISCUSSION

In order to mimic the properties of FRB 20191001A (Figure 1c), we adopt a “single-component” envelope (Table 2 of Scott *et al.* 2025), implying an intrinsic FWHM  $W_0 \sim 0.5$  ms

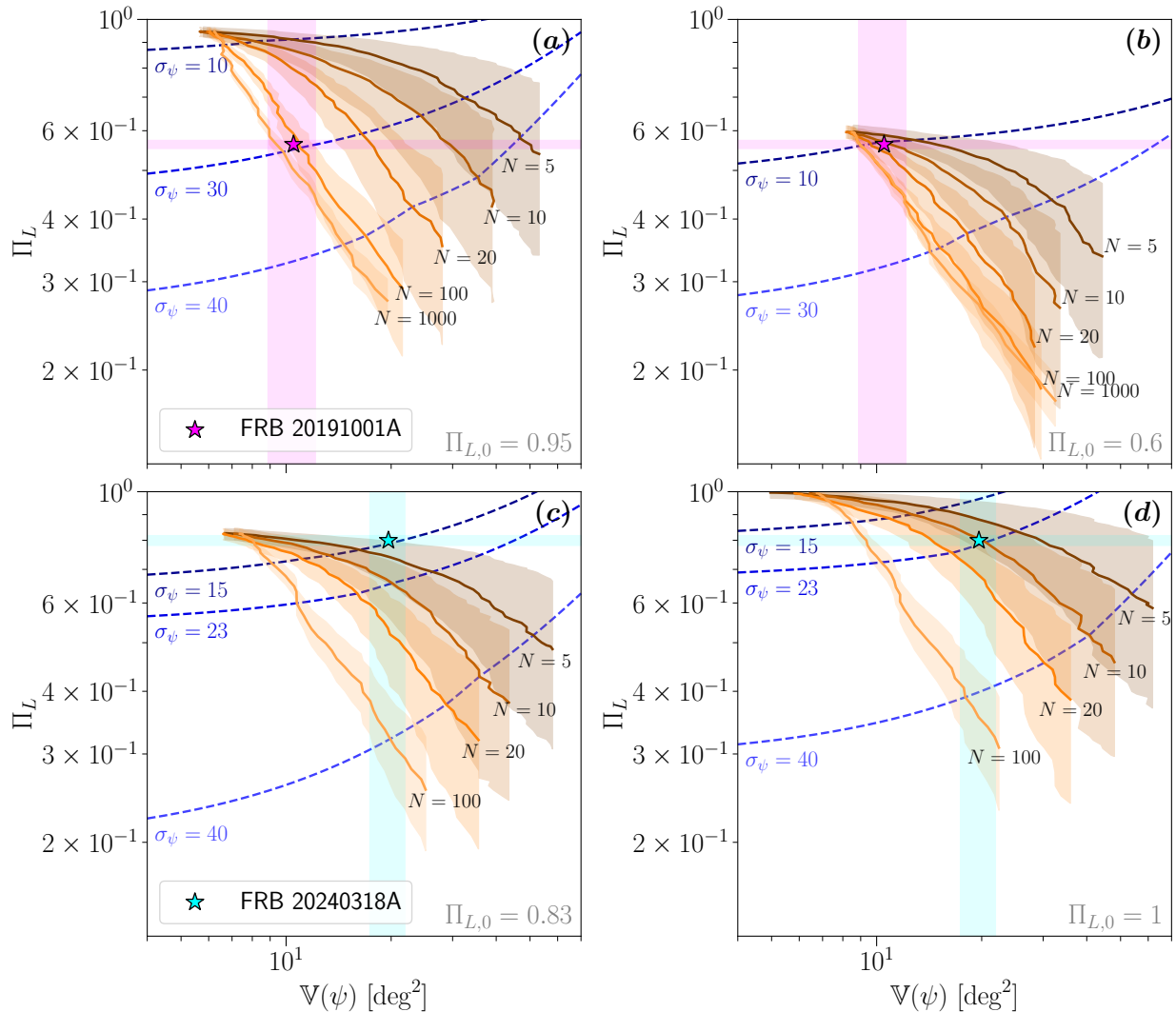


**Figure 3.** Measured linear polarisation fraction,  $\Pi_L$ , versus measured PA variance,  $\mathbb{V}(\psi)$ , as a function of the standard deviation of the intrinsic microshot PA,  $\sigma_\psi$ , for the leading phases of the mock FRB 20191001A (panels (a)–(b) with intrinsic linear polarisation fractions  $\Pi_{L,0} = 0.95$  and  $0.6$ , respectively) and FRB 20240318A (panels (c)–(d),  $\Pi_{L,0} = 0.83$  and  $1$ ). For  $N = 5, 10, 20, 100$  microshots, at each  $\sigma_\psi$  we generate 500 random realisations of each FRB with fixed S/N (FRB 20191001A: median  $\sim 174$ ; FRB 20240318A: median  $\sim 110$ ) and plot the medians of the  $\Pi_L$  and  $\mathbb{V}(\psi)$  distributions as solid lines. The shaded regions mark the 16th–84th percentiles of the  $\Pi_L$  distributions. The magenta and cyan stars show the measured values for FRB 20191001A and FRB 20240318A, respectively (see Figures 1d and 4b), with shaded bands indicating errors from off-pulse RMS noise. Blue dashed lines connect points of constant  $\sigma_\psi$  and are linearly extended using the slopes of their first and last segments (FRB 20191001A:  $\sigma_\psi = 10^\circ, 30^\circ, 40^\circ$ ; FRB 20240318A:  $\sigma_\psi = 15^\circ, 23^\circ, 40^\circ$ ).

given the measured scattering timescale  $\tau_{1\text{ GHz}} = 1.78$  ms. For an illustrative choice of  $N = 100$  microshots with intrinsic linear polarisation fraction  $\Pi_{L,0} = 0.95$  arriving within  $W_0$ , matching the observed linear polarisation fraction requires  $\sigma_\psi \sim 30^\circ$  (Figure 3a). As demonstrated in Figures 1 and 2, superposition of microshots with differing intrinsic PAs naturally produces a time-variable PA profile, while scattering preferentially suppresses this variability on the trailing edge, broadly consistent with observations (Scott et al., 2025).

Scattering, however, is not the sole mechanism that suppresses observable PA structure. Finite instrumental sampling further averages intrinsic PA fluctuations: when the sampling time  $\delta t$  exceeds the characteristic microshot separation, rapid PA variations are smoothed, yielding an apparently flat PA

profile even for relatively large  $\sigma_\psi$ . As a result, configurations with low  $N$  and large intrinsic PA dispersion are strongly disfavoured only when both the scattering timescale and the sampling time are short enough to preserve intrinsic variability. Otherwise, intrinsic PA structure is efficiently averaged out prior to measurement.

The absence of any observed correlation between reductions in linear polarisation fraction and PA fluctuations (Scott et al., 2025) therefore disfavours strong intrinsic depolarisation arising purely from large PA dispersion at fixed, low  $N$ , but does not uniquely exclude high- $\sigma_\psi$  configurations. The data remain consistent with either (i) large  $\sigma_\psi$  combined with sufficiently large  $N$ , such that PA variations average out through superposition, scattering, and finite sampling, or (ii) smaller

intrinsic  $\sigma_\psi$  with  $N$  constrained by the measured PA variance. Importantly, apparent PA fluctuations in the scattering tail should not be interpreted as physically meaningful unless they are detected at sufficiently high S/N, as noise-dominated regions can spuriously inflate  $\mathbb{V}(\psi)$  (Section 3.1). The observed behaviour therefore reflects a coupled degeneracy between  $\sigma_\psi$ ,  $N$ ,  $\tau$ ,  $\delta t$ , and S/N.

This degeneracy is illustrated in Section 3.2, where all simulations converge to identical  $\Pi_L$  and  $\mathbb{V}(\psi)$  at  $\sigma_\psi = 0$  (Figure 3). Shifts in  $\mathbb{V}(\psi)$  require changes in the effective S/N: increasing S/N reduces the measured PA variance, while decreasing the S/N of the linearly polarised intensity  $L$  (lowering  $\Pi_{L,0}$ ) increases the contribution of noise to  $\mathbb{V}(\psi)$ . The measured values for FRB 20191001A (Figure 1d) therefore do not uniquely select a single intrinsic configuration, but instead constrain an allowed region of  $(N, \sigma_\psi, \Pi_{L,0})$  space.

Within this framework, Figure 3a shows that reproducing the observed properties of FRB 20191001A with a high intrinsic linear fraction ( $\Pi_{L,0} = 0.95$ ) favours intrinsic PA dispersions of order  $\sigma_\psi \sim 30^\circ$  when the number of microshots is  $N \gtrsim 100$ . This reflects efficient averaging of intrinsically misaligned PAs through microshot superposition, scattering, and finite instrumental sampling. However, once these averaging effects and the contribution of noise are accounted for, comparable levels of measured PA variance can also be obtained without invoking such large intrinsic dispersions. In particular, Figure 3b demonstrates that reducing the intrinsic linear fraction to  $\Pi_{L,0} = 0.6$  allows models with more modest PA dispersion ( $\sigma_\psi \sim 10^\circ$ ) and  $N \gtrsim 10$  to reproduce the observations. Larger values of  $N$  combined with slightly reduced  $\Pi_{L,0}$  and smaller  $\sigma_\psi$  remain equally consistent. Taken together, the data for FRB 20191001A are best described by a broad region of parameter space in which modest intrinsic PA dispersion is compatible with the observed near-constant PA once instrumental resolution, propagation effects, and noise statistics are properly incorporated (Scott *et al.*, 2025).

By contrast, FRB 20240318A exhibits a genuinely variable PA trend (Scott *et al.*, 2025). Assuming a fully linearly polarised intrinsic signal ( $\Pi_{L,0} = 1$ ), Figure 3d allows configurations with  $N = 5\text{--}20$  and intrinsic PA dispersion  $\sigma_\psi \sim 23^\circ$ . Relaxing this assumption to  $\Pi_{L,0} = 0.83$  with  $\Pi_{V,0} = -0.17$  shifts the allowed region toward fewer microshots, with Figure 3c favouring  $N \leq 5$  and more modest PA dispersion ( $\sigma_\psi \sim 15^\circ$ ). These solutions occupy a different part of the same  $(N, \sigma_\psi, \Pi_{L,0})$  space explored for FRB 20191001A, rather than requiring a fundamentally larger intrinsic PA dispersion. The observed PA variability therefore reflects a combination of reduced microshot averaging and intrinsic PA structure, rather than uniquely implying broader intrinsic PA distributions.

A key limitation of the present analysis is the use of PA variance as the primary diagnostic of intrinsic structure. Variance is not sensitive to how the PA varies in time, encoding neither coherence, intermittency, nor ordered swings. Consequently, distinct PA behaviours can yield similar  $\mathbb{V}(\psi)$ , particularly in noise-dominated or temporally averaged regimes. Structure-based metrics that explicitly quantify PA organisation (e.g., Scott *et al.*, 2025) are therefore likely to provide a more infor-

mative and robust characterisation of intrinsic PA behaviour than variance alone. Future extensions of FIRES will incorporate such measures.

Finally, comparisons between FRB microstructure and Galactic pulsars such as the Crab must be interpreted cautiously. The extreme PA swings observed in Crab nanoshots occur on nanosecond timescales and would be strongly averaged out at the millisecond-to-microsecond resolutions of current FRB observations. As a result, present data probe only a temporally averaged manifestation of any underlying nanoshot structure, and unresolved Crab-like PA variability in FRBs cannot be ruled out. Apparent differences in polarimetric behaviour may therefore reflect observational limitations rather than fundamentally distinct emission physics.

#### 4.1 Future Model Considerations

The present iteration of FIRES lacks several physical ingredients that will be incorporated into future versions:

- **Multiple scattering and scintillation screens:** Currently only a single thin-screen model is implemented, preventing realistic modelling of multi-path propagation and frequency-dependent scintillation structure.
- **Thick-screen scattering:** The code assumes an infinitely thin screen, whereas a volumetric or extended medium would alter temporal broadening and pulse-shape evolution.
- **Generalised Faraday rotation:** FIRES uses standard Faraday rotation, but cannot yet capture mode-coupling or birefringent effects expected in magnetised, relativistic plasmas.

#### 5. Conclusions

We have introduced FIRES, a simple, emission-mechanism-independent framework for modelling FRB dynamic spectra as the incoherent superposition of Gaussian microshots, followed by thin-screen scattering, diffractive scintillation, and Gaussian noise.

Applied to the CRAFT FRBs 20191001A and 20240318A, FIRES reproduces key polarimetric behaviours (Figures 1 and 4): scattering suppresses PA variability on the trailing edge, while the leading edge preferentially preserves intrinsic PA structure provided that sufficient signal-to-noise is present. We quantify this behaviour using the PA variance ratio  $\mathcal{R}_\psi$  (Equation (5)) and expectations from the low-scattering, high-S/N regime. Depolarisation arises naturally from incoherent microshot superposition: increasing either the number of microshots  $N$  or the intrinsic PA dispersion  $\sigma_\psi$  reduces the observed linear polarisation fraction while narrowing the intrinsic PA variance, whereas lower intrinsic linear fraction  $\Pi_{L,0}$  increases the relative contribution of noise and inflates the measured PA variance (Figure 3). These effects define a degenerate but bounded region of parameter space rather than a unique solution.

For FRB 20191001A, the data are consistent with an extended region of parameter space spanning  $\sigma_\psi \sim 10^\circ\text{--}30^\circ$  and  $N \sim 5\text{--}1000$ , reflecting trade-offs between intrinsic PA

dispersion, microshot number, scattering, finite sampling, and signal-to-noise. FRB 20240318A occupies a different part of this same parameter space, with its observed PA variability favouring solutions involving fewer microshots and reduced averaging, rather than uniquely requiring larger intrinsic PA dispersion. In both bursts, configurations with modest intrinsic  $\sigma_\psi$  remain viable once instrumental resolution, scattering, and noise contributions are accounted for, and current data do not demand fundamentally distinct intrinsic PA statistics between the two sources.

We stress that apparent differences between FRB polarimetric behaviour and that of Galactic pulsars, such as the Crab, must be interpreted with caution. The extreme PA swings observed in Crab nanoshots occur on nanosecond timescales and would be strongly averaged out at the millisecond-to-microsecond resolutions of current FRB observations. As a result, existing FRB data probe only a temporally averaged manifestation of any underlying nanoshot structure, and unresolved Crab-like PA variability remains observationally unconstrained rather than excluded.

More generally, PA variance alone is an incomplete statistic: it quantifies the spread of PA values but not how the PA varies in time, and it is highly susceptible to noise in low-S/N regions such as scattering tails. Apparent PA fluctuations in these regions should therefore not be over-interpreted unless supported by sufficient signal. More informative structure-sensitive diagnostics, such as correlation-based or scale-dependent measures, will be required to robustly characterise intrinsic PA evolution.

Overall, the leading-edge window and higher-frequency sub-bands provide the most reliable access to intrinsic PA information, and the joint plane of  $\Pi_L$  versus PA variance offers a compact, physically interpretable summary of the allowed  $(N, \sigma_\psi, \Pi_{L,0})$  parameter space at fixed S/N. Future FRB observations at substantially higher time resolution and sensitivity will be essential to break these degeneracies and directly test whether FRBs exhibit Crab-like nanoshot PA variability on unresolved timescales.

Future work will extend FIRES in two directions. On the modelling side, we will incorporate multiple and thick scattering screens, generalised Faraday rotation, and intrinsic spectral structure to better reflect realistic propagation environments. Observationally, we will apply the framework to high-time-resolution, low-scattering ( $\tau \ll W$ ) FRBs, where intrinsic microstructure is only weakly distorted. By forward-modelling such bursts directly in the dynamic-spectral and polarimetric domains, we will test whether FIRES can reliably recover intrinsic microshot properties—including  $N$ ,  $\sigma_\psi$ , and  $\Pi_{L,0}$ —from real data.

## Acknowledgement

This research was supported by an Australian Government Research Training Program (RTP) Scholarship (<https://doi.org/10.82133/C42F-K220>).

## References

- Beniamini, P., & Kumar, P. 2020, MNRAS, 498, 651
- Bera, A., James, C. W., Deller, A. T., et al. 2024, ApJ, 969, L29
- Cordes, J. M. 1976, ApJ, 210, 780
- Day, C. K., Deller, A. T., Shannon, R. M., et al. 2020, MNRAS, 497, 3335
- Everett, J. E., & Weisberg, J. M. 2001, ApJ, 553, 341
- Feng, Y., Li, D., Yang, Y.-P., et al. 2022, Science, 375, 1266
- Gupta, V., Flynn, C., Farah, W., et al. 2022, MNRAS, 514, 5866
- Hankins, T. H., & Eilek, J. A. 2007, ApJ, 670, 693
- Hankins, T. H., Eilek, J. A., & Jones, G. 2016, ApJ, 833, 47
- Hankins, T. H., Jones, G., & Eilek, J. A. 2015, ApJ, 802, 130
- Hazboun, J., Shapiro-Albert, B., Baker, P., et al. 2021, The Journal of Open Source Software, 6, 2757
- Hewitt, D. M., Hessels, J. W. T., Ould-Boukattine, O. S., et al. 2023, MNRAS, 526, 2039
- Hotan, A. W., van Straten, W., & Manchester, R. N. 2004, PASA, 21, 302
- Jessner, A., Popov, M. V., Kondratiev, V. I., et al. 2010, A&A, 524, A60
- Li, X. H., & Han, J. L. 2003, A&A, 410, 253
- Lorimer, D. R., Bailes, M., McLaughlin, M. A., Narkevic, D. J., & Crawford, F. 2007, Science, 318, 777
- Luo, R., Wang, B. J., Men, Y. P., et al. 2020, Nature, 586, 693
- McKinnon, M. M. 2006, ApJ, 645, 551
- Mckinven, R., Bhardwaj, M., Eftekhar, T., et al. 2025, Nature, 637, 43
- Melrose, D. B., & Macquart, J. P. 1998, ApJ, 505, 921
- Nimmo, K., Hessels, J. W. T., Keimpema, A., et al. 2021, Nature Astronomy, 5, 594
- Nimmo, K., Hessels, J. W. T., Kirsten, F., et al. 2022, Nature Astronomy, 6, 393
- Osłowski, S., van Straten, W., Hobbs, G. B., Bailes, M., & Demorest, P. 2011, MNRAS, 418, 1258
- Pandhi, A., Pleunis, Z., Mckinven, R., et al. 2024, ApJ, 968, 50
- Petroff, E., Hessels, J. W. T., & Lorimer, D. R. 2019, A&A Rev., 27, 4
- . 2022, A&A Rev., 30, 2
- Pleunis, Z., Good, D. C., Kaspi, V. M., et al. 2021, ApJ, 923, 1
- Rickett, B. J. 1975, ApJ, 197, 185
- Sand, K. R., Curtin, A. P., Michilli, D., et al. 2025, ApJ, 979, 160
- Scott, D. R., Dial, T., Bera, A., et al. 2025, arXiv e-prints, arXiv:2505.17497
- Sherman, M. B., Connor, L., Ravi, V., et al. 2024, ApJ, 964, 131
- Snelders, M. P., Nimmo, K., Hessels, J. W. T., et al. 2023, Nature Astronomy, 7, 1486
- Uttarkar, P. A., Shannon, R. M., Gourdji, K., et al. 2025, arXiv e-prints, arXiv:2503.19749

### Appendix 1. Back-of-the-envelope derivation of the expected variance of the polarisation angle

We give a sanity check for the expected variance of the polarisation angle (PA) under the microshot model introduced in the main text. Let the envelope have FWHM  $W_0$  (ms) and each microshot have FWHM  $w_i = f_i W_0$ , where  $f_i \in [f_{\min}, f_{\max}]$ . For an order-of-magnitude estimate we replace the width fraction by its mean

$$f_w = \frac{1}{2}(f_{\min} + f_{\max}), \quad w \equiv f_w W_0.$$

Write  $\kappa \equiv 2\sqrt{2\log 2}$  so that FWHM  $\rightarrow \sigma$  via  $\sigma = \text{FWHM}/\kappa$ . A thin-screen exponential scattering response with timescale  $\tau$  (ms) broadens Gaussian widths in quadrature,

$$\sigma_{W,\text{tot}} = \sqrt{\sigma_W^2 + \tau^2}, \quad \sigma_{w,\text{tot}} = \sqrt{\sigma_w^2 + \tau^2},$$

with  $\sigma_W = W_0/\kappa$  and  $\sigma_w = w/\kappa$ . The corresponding broadened FWHM measures are

$$W_{\text{tot}} = \kappa \sigma_{W,\text{tot}}, \quad w_{\text{tot}} = \kappa \sigma_{w,\text{tot}}.$$

If  $N$  microshots occur within the envelope, the number that effectively contribute at any time scales with the broadened-width ratio. Defining

$$r \equiv \frac{w_{\text{tot}}}{W_{\text{tot}}} = \frac{\sigma_{w,\text{tot}}}{\sigma_{W,\text{tot}}}, \quad N_{\text{eff}} = N r,$$

and letting  $\sigma_\psi$  be the intrinsic single-shot PA scatter (radians), the rms PA scatter is

$$\psi_{\text{rms}} \approx \frac{\sigma_\psi}{\sqrt{N_{\text{eff}}}}, \quad (7)$$

so the basic variance estimate is

$$\mathbb{V}_{\text{exp}}(\psi) = \psi_{\text{rms}}^2 = \frac{\sigma_\psi^2}{N r} = \frac{\sigma_\psi^2 W_{\text{tot}}}{N w_{\text{tot}}}. \quad (8)$$

When estimating fluctuations about the mean PA across the envelope, subtracting the mean introduces a degrees-of-freedom correction. Approximating the number of independent samples by  $M \approx W_{\text{tot}}/w_{\text{tot}} = 1/r$  gives  $(M-1)/M \approx 1-r$ , yielding

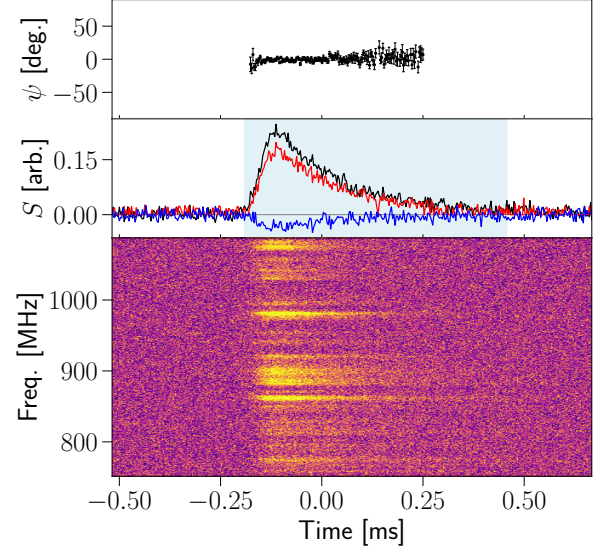
$$\mathbb{V}_{\text{exp}}(\psi) = \frac{\sigma_\psi^2}{N r} (1-r) = \frac{\sigma_\psi^2 W_{\text{tot}}}{N w_{\text{tot}}} \left(1 - \frac{w_{\text{tot}}}{W_{\text{tot}}}\right). \quad (9)$$

Simplifying and converting to deg<sup>2</sup>,

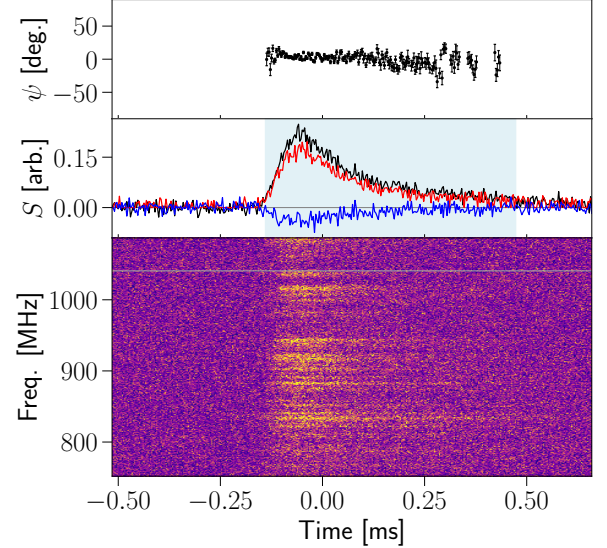
$$\mathbb{V}_{\text{exp}}(\psi) = \frac{\sigma_\psi^2}{N} \left( \frac{W_{\text{tot}}}{w_{\text{tot}}} - 1 \right) \left( \frac{180}{\pi} \right)^2. \quad (10)$$

This corrected estimate tends to zero as scattering grows large ( $r \rightarrow 1$ ). It ignores amplitude weighting, detailed temporal structure, and the full width distribution, but provides a rapid order-of-magnitude check. If needed for discretely sampled data with time resolution  $\delta t$ , one may downweight  $N_{\text{eff}}$  by  $\min(1, \sigma_{w,\text{tot}}/(\delta t/\kappa))$  to account for unresolved microshots.

### Appendix 2. FRB 20240318A



(a) FIRES



(b) FRB 20240318A

**Figure 4.** A FIRES recreation of FRB 20240318A. Top: A FIRES recreation of FRB 20240318A comprised of 100 microshots,  $\tau_{1\text{ GHz}} = 0.128$  ms and scintillation (on-pulse S/N= 109). Bottom: real FRB 20240318A data reproduced from Scott *et al.* (2025) (on-pulse S/N= 109, RM corrected from RM= 48.06 rad m<sup>-2</sup>). The full list of parameters used are presented in Table 1 and are described in Section 2. The top panels show the polarisation angle, the centre panels show the pulse profile, and the bottom panels show the dynamic spectra. The blue shaded regions in the centre panels is the minimum boxcar width that contains 95% of the total flux in the pulse profile.